




# Integrated SQUID/Sensor Metallic Magnetic Microcalorimeter for Gamma-Ray Spectroscopy

S. T. P. Boyd<sup>1</sup>  · R. Hummatov<sup>1</sup> · G. B. Kim<sup>2</sup> · L. N. Le<sup>1</sup> · J. A. Hall<sup>3</sup> · R. Cantor<sup>3</sup> · S. Friedrich<sup>2</sup>

Received: 5 November 2017 / Accepted: 25 June 2018 / Published online: 3 July 2018  
© Springer Science+Business Media, LLC, part of Springer Nature 2018

## Abstract

Metallic magnetic microcalorimeters (MMCs) achieve energy resolution comparable to transition-edge sensors (TESs) but rely on different measurement physics that may allow MMCs to surpass TESs in some future applications. We have recently completed fabrication of new MMC  $\gamma$ -ray detector arrays using several exploratory sensor designs. All designs integrate the SQUID and sensor on the same chip and use a superconducting cap layer on the paramagnet, but explore different combinations of combined/separate sensing and magnetization coils and direct/flux transformer coupling to the input SQUIDs. This report describes the design and initial testing of one of these devices, which has so far demonstrated an energy resolution of 38 eV at 60 keV near 10 mK using natural-abundance silver–erbium paramagnet.

**Keywords** MMC · Metallic magnetic calorimeter · Gamma-ray spectroscopy

## 1 Introduction

Gamma-ray detectors based on metallic magnetic calorimeters (MMCs) offer energy resolution an order of magnitude better than high-purity germanium (HPGe) detectors that are currently used for gamma spectroscopy of nuclear materials [1–6]. This can increase the accuracy of nondestructive assay (NDA) in applications where HPGe detectors are affected by line overlap. In addition, MMCs have a reproducible response function that allows simple detector calibration [7] and are therefore well suited to improve the accuracy of the nuclear data that NDA is based on.

---

✉ S. T. P. Boyd  
stpboyd@gmail.com

<sup>1</sup> University of New Mexico, Albuquerque, NM 87131, USA

<sup>2</sup> Lawrence Livermore National Laboratory, Livermore, CA 94550, USA

<sup>3</sup> STAR Cryoelectronics, Santa Fe, NM 87508, USA

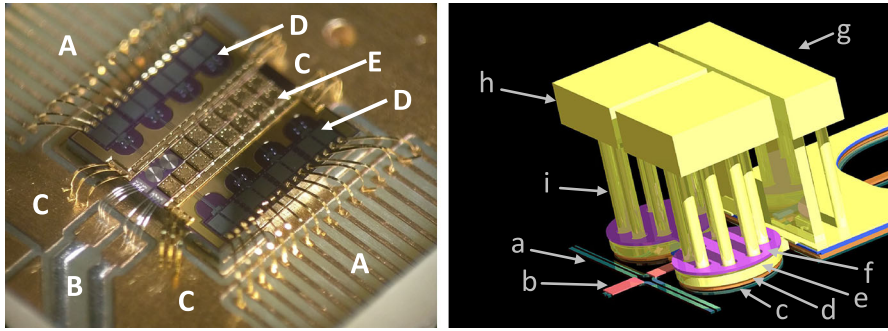


**Fig. 1** (Left) 14-pixel MMC array on its circuit board carrier. The chip is 5 mm  $\times$  5 mm. (A) Gold ribbon bonds connect bias and feedback for the 8-input SQUIDs, (B) aluminum bonds connect the two pads of the common magnetizing circuit, (C) gold ribbon bonds provide thermal anchoring at the four ends of the two elevated thermal busses, (D) input SQUIDs, (E) 14 absorbers, each 475  $\mu\text{m}$   $\times$  475  $\mu\text{m}$   $\times$  30  $\mu\text{m}$  thick. The two positions without absorbers at the end of one row are an on-chip thermometer that was not used in these tests. (Right) Detail of the two gradiometric sensors and absorbers connected to each input SQUID (not to scale, vertical scale is greatly exaggerated): (a) Common magnetizing circuit, (b) passive persistent-current switches, (c) magnetizing coil, (d) sensing coil, (e) Ag:Er 1000 at. ppm paramagnet made with natural-abundance Er, (f) superconducting cap, (g) the elevated thermal bus is formed in the same processing steps as the absorbers and posts, and creates a high-conductance path to bring the anchor temperature to the cold side of each pixel's weak thermal link, (h) gold absorber, (i) gold posts connect to the gold thermalization layer on top of the paramagnet through holes in the superconducting cap. The heat flow path from the absorber out to the circuit board carrier and cryostat is entirely high-conductivity normal metal for good conduction at low-mK temperatures (Color figure online)

We have recently completed fabrication of new MMC  $\gamma$ -ray detector arrays using several exploratory integrated SQUID/sensor designs. Integration of the SQUID and sensing coil on the same chip allows optimal inductance matching and control of stray reactances. These designs explore different combinations of one-layer/two-layer sensing coils and direct/flux transformer coupling of the input circuits. All designs use the Meissner effect of a superconducting Nb cap layer to confine the magnetizing field to the paramagnet and to reduce the sensing coil inductance. In this report, we describe the design and initial testing of one of these exploratory devices.

## 2 Design

An overview of the MMC array described in this report, together with some details of the sensor geometry and heat flow path, is given in Fig. 1. Devices were fabricated using a modified version of the commercial STAR Cryo “Delta 1000” SQUID process, followed by cm-scale chip processing using clean rooms at both STAR Cryo and UNM. Additional information about fabrication is provided in [8].

An electrical schematic for the tested pixel design and readout is shown in Fig. 2 left. This design is configured as a transformer-coupled series gradiometer with a separate magnetizing circuit (“two-layer sensing coil”). Readout is via a commercial STAR Cryo SQUID array and PFL-102 direct-readout flux-locked-loop electronics.

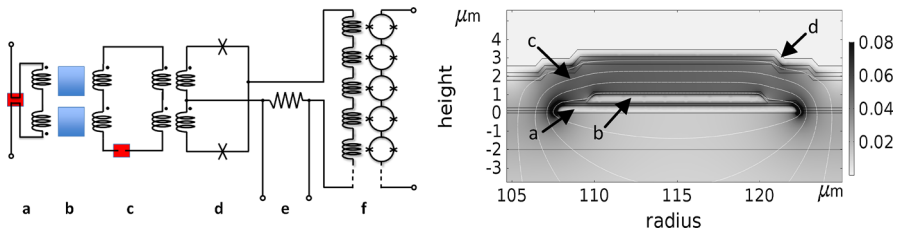


**Fig. 2** (Left) Schematic of the SQUID/sensor and readout: (a) magnetizing circuit, (b) paramagnet, (c) flux transformer, (d) input SQUID, (e) bias resistor for input SQUID, (f) series SQUID array amplifier. The small rectangles connecting wires represent passive persistent-current switches. Components (a–d) make up one integrated SQUID/sensor providing two pixels on the MMC array chip. Components (e–f) are on a separate chip mounted on the 3.5 K stage. (Right) Cross-section detail of one turn of the sensing coil geometry: (a) magnetizing coil trace, (b) sensing coil trace, (c) paramagnet, (d) superconducting Nb cap. Shading in the paramagnet shows the calculated magnetizing field magnitude in units of T/A, showing the confinement of the field by the superconducting cap (Color figure online)

A key part of MMC performance optimization is maximizing the flux change induced in the input SQUID, where the measurement is made, per flux change that the paramagnet induces in the sensing coil when the particle’s energy is absorbed. From the schematic in Fig. 2 left, it is easy to show that this flux transfer ratio is given by

$$\frac{\Delta\phi_{\text{SQUID}}}{\Delta\phi_{\text{sensor}}} = \frac{2k\sqrt{L_{\text{primary}}L_{\text{secondary}}}}{2(L_{\text{sensor}} + L_{\text{primary}}) + L_{\text{parasitic}}},$$

where  $L_{\text{sensor}}$  is the inductance of each of the two sensing coils on the left side of the flux transformer, and  $L_{\text{primary}}$  is the inductance of each of the two input transformer primaries on the right side of the flux transformer.  $L_{\text{secondary}}$  is the inductance of each of the two input transformer secondaries, the sum of which makes up the unscreened SQUID loop inductance  $L_{\text{SQUID}}$ .  $k$  is the mutual inductance coupling factor for each input transformer.  $L_{\text{parasitic}}$  is the sum of any inductances in the flux transformer loop outside the sensing coils or the input transformer primaries.

It is also easy to show that this flux transfer is maximized when  $L_{\text{primary}} = L_{\text{sensor}} + L_{\text{parasitic}}/2$ . Assuming this condition can be engineered, if we then write  $L_{\text{sensor}} = \alpha L_{\text{SQUID}}$ , and  $L_{\text{parasitic}} = \beta L_{\text{SQUID}}$ , the optimal flux transfer is  $\Delta\phi_{\text{SQUID}}/\Delta\phi_{\text{sensor}}|_{\text{optimal}} = k/(2\sqrt{2\alpha + \beta})$ .

Thus it is always desirable in this circuit topology to minimize  $L_{\text{parasitic}}$  and to maximize  $k$ . Because the design of the sensing coil affects both  $\Delta\phi_{\text{sensor}}$  and  $\alpha$ , we also wish to maximize the quantity  $\Delta\phi_{\text{sensor}}/\sqrt{\alpha}$ .

The lowest values of  $L_{\text{parasitic}}$  are achieved when the sensing coils and the input SQUID are integrated on the same chip. This allows the use of microstrip wiring geometries to connect the input transformers and sensing coils, achieving very low  $L_{\text{parasitic}}$  even if they are some distance from each other. In this design, the separation is about 1 mm, and we estimate  $L_{\text{parasitic}}$  to be only about 9.5 pH ( $\beta \approx 0.05$ ). Good control of  $L_{\text{parasitic}}$  becomes increasingly important for low-inductance sensing coils such as those that use a superconducting cap.

The inductance values required for the flux transfer calculation can be estimated with good accuracy from the trace geometries. For this device, we estimate  $L_{\text{sensor}} = 955$  pH,  $L_{\text{primary}} = 892$  pH,  $L_{\text{secondary}} = 100$  pH, and  $L_{\text{parasitic}} = 9.5$  pH. The mutual coupling constant  $k$  can be determined by comparing the measured feedback mutual inductance (feedback current in this design flows through one of the input transformer secondaries) to the estimated  $L_{\text{secondary}}$ . This determines the degree of flux screening caused by the superconducting flux transformer loop, from which we find  $k = 0.85$ . The overall flux transfer ratio is then found to be 0.137. This is about 85% of the optimal flux coupling that can be achieved for  $k = 1$  and  $\beta = 0$  with these  $L_{\text{sensor}}$  and  $L_{\text{SQUID}}$  values. Thus  $k = 0.85$  is the main source of inefficiency.

The passive persistent-current switches indicated in Fig. 2 left are a novel feature of our MMC devices. They provide a simple solution to the problem of trapping persistent magnetizing currents into many superconducting loops on the MMC chip without the layout complexity and potential for noise coupling if electrically heated persistent-current switches were used. We have previously described our development and use of passive switches based on Nb/Ta bilayers [9]. The passive switches used in this design are an improved version based on Nb/Ta alloy that we plan to describe in a future publication.

Another novel feature in Fig. 2 left is the use of a separate magnetizing circuit, which was included in this design to avoid the introduction of large currents into the SQUID input transformers. Although a parallel, rather than series, gradiometer design could have avoided this requirement, gaining experience with separate magnetizing circuits is a high priority for our group, as a separate magnetizing circuit may be required to ensure adequate decoupling of the input SQUIDs from each other and from any noise in the common magnetizing circuit in future high-performing direct-coupled MMC arrays. Although the sensitivity of the MMC sensing coil is always maximized when the magnetizing current flows through the sensing coil itself, our calculations indicate that the penalty for a separate magnetizing circuit can be as low as a few percent in optimized geometries.

Figure 2 right shows a detail from a 2D axisymmetric cross section of the two-layer sensing coil. The separate magnetizing coil is configured as a planar spiral meander, i.e., a bifilar spiral with the two traces connected in the middle. Round coil geometries are well approximated in 2D axisymmetry, allowing rapid and accurate finite element calculations. Although the spiral meander performs somewhat less well than a true spiral in the superconducting cap configuration, the use of a meander in this design permits a magnetizing circuit without vias or crossovers, increasing yield for these exploratory devices and allowing larger on-chip magnetizing currents. The sensing coil is configured as a second meander with the same pitch and number of turns (but narrower traces) atop the magnetizing coil, separated by about 150 nm of SiO<sub>2</sub> for electrical insulation.

The superconducting cap [10] provides several benefits through its Meissner effect diamagnetism: (1) The image currents in the cap effectively form a microstrip geometry with the coils that largely confines the magnetic field between the cap and the coils. This increases the fraction of the magnetic field energy inside the volume of the paramagnet and increases the signal. (2) The effective microstrip geometry also reduces  $L_{\text{sensor}}$ . This reduction is typically a factor of  $\sim 2$  for meander coils but can be greater than

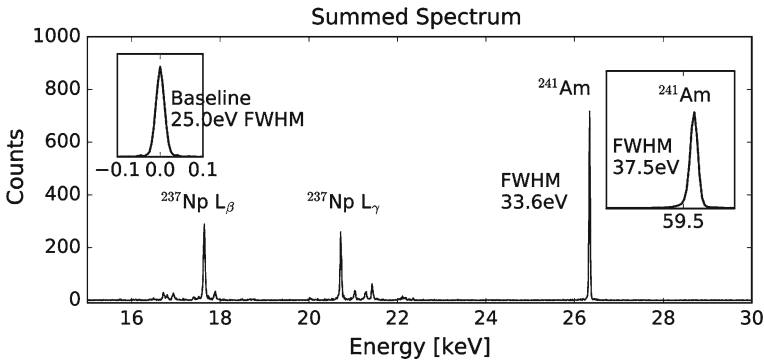


Fig. 3 Gamma-ray spectrum obtained with  $^{241}\text{Am}$

an order of magnitude for spiral coils. Benefits (1) and (2) both act to increase the figure of merit  $\Delta\phi_{\text{sensor}}/\sqrt{\alpha}$  for this device, and both are also important for good performance in future direct-coupled devices. (3) The field confinement essentially eliminates magnetic cross talk between pixels. Uncapped meanders, even if they are configured to have zero dipole moment overall, will typically retain some level of coupling to nearby traces and pixels.

### 3 Performance

A recent gamma-ray spectrum taken with this device is shown in Fig. 3. We limited the trapped magnetizing current to 95 mA to avoid quenching the magnetizing circuit due to heating in the resistive pin connections. Although the temperature of the BlueFors LD400 dilution refrigerator was regulated at 10 mK for this test, we estimate that the detector was likely operating around  $\sim 20$  mK because the MMC signal stopped increasing below that temperature. This is likely due to heating by the first-stage SQUID and the Kapton insulation between the detector holder and the mixing chamber that we added to reduce electromagnetic interference.

The  $^{241}\text{Am}$  source was external to the cryostat and irradiated the detector through thin windows. The MMC input SQUID was read out (see Fig. 2 left) with a STAR Cryo AR232-16 SQUID array amplifier and PFL-102 readout electronics, then low-pass filtered with 1 MHz bandwidth. The filtered signals were sampled at 2 MS/s with a 16-bit GaGe digitizer. Six-millisecond-long waveforms were processed by a trapezoidal filter using a 0.9-ms peaking time and a 2.5- $\mu\text{s}$  gap time. The positive-going and negative-going signals from the two gradiometric sensors (see Fig. 2 left) were linearly calibrated separately, using the  $^{241}\text{Am}$  lines at 26.3 and 59.5 keV. The two calibrated spectra were then summed to produce the spectrum in Fig. 3.

The energy resolution of 37.5 eV FWHM at 60 keV, obtained with an exploratory design and using lower-performing natural-abundance Er in the paramagnetic sensor, already has a value between the best reported single-pixel gamma-ray performance for a TES microcalorimeter, 22 eV FWHM at 97 keV [6], and the 55 eV average FWHM measured across a 256-pixel TES array [5]. Rodrigues et al. [3] have recently reported

23.5 eV FWHM best-pixel performance for an MMC optimized for constant detection efficiency at lower energies between 5 and 26 keV. The energy resolution of the device reported here near 26 keV is 33.6 eV FWHM (Fig. 3). Since the SQUID noise in our measurements was a comparably high  $\sim 6 \mu\Phi_0/\sqrt{\text{Hz}}$ , energy resolution can be further improved. This is the subject of current work.

**Acknowledgements** S.B. thanks the UNM Center for Advanced Research Computing for their ongoing support. This work was funded by the U.S. DOE Office of Non-proliferation R&D (NA-22) under Grant LL16-MagMicro-PD2La. It was performed under the auspices of the U.S. Department of Energy by Lawrence Livermore National Laboratory under Contract DE-AC52-07NA27344.

## References

1. D. Hengstler, M. Keller, C. Schötz, J. Geist, M. Krantz, S. Kempf, L. Gastaldo, A. Fleischmann, T. Gassner, G. Weber, R. Martin, Th Stöhlker, C. Enss, *Phys. Scr.* **2015**, 014054 (2015). <https://doi.org/10.1088/0031-8949/2015/t166/014054>
2. C. Bates, C. Pies, S. Kempf, D. Hengstler, A. Fleischmann, L. Gastaldo, C. Enss, S. Friedrich, *J. Low Temp. Phys.* **184**, 351–355 (2016). <https://doi.org/10.1007/s10909-015-1348-0>
3. M. Rodrigues, R. Mariam, M. Loidl, *EPJ Web Conf.* **146**, 10012 (2017). <https://doi.org/10.1051/epjconf/201714610012>
4. A. Fleischmann, C. Enss, G.M. Seidel, *Metallic magnetic calorimeters*, in *Cryogenic Particle Detection*, ed. by C. Enss (Springer, Berlin, 2005), pp. 151–216
5. R. Winkler, A.S. Hoover, M.W. Rabin, D.A. Bennett, W.B. Doriese, J.W. Fowler, J. Hays-Wehle, R.D. Horansky, C.D. Reintsema, D.R. Schmidt, L.R. Vale, J.N. Ullom, *Nucl. Instrum. Methods A* **770**, 203–210 (2015). <https://doi.org/10.1016/j.nima.2014.09.049>
6. M.K. Bacrania, A.S. Hoover, P.J. Karpus, M.W. Rabin, C.R. Rudy, D.T. Vo, J.A. Beall, D.A. Bennett, W.B. Doriese, G.C. Hilton, R.D. Horansky, K.D. Irwin, N. Jethava, E. Sassi, J.N. Ullom, L.R. Vale, *IEEE Trans. Nucl. Sci.* **56**(4), 2299–2302 (2009). <https://doi.org/10.1109/TNS.2009.2022754>
7. C.R. Bates, C. Pies, S. Kempf, D. Hengstler, A. Fleischmann, L. Gastaldo, C. Enss, S. Friedrich, *Appl. Phys. Lett.* **109**, 023513 (2016). <https://doi.org/10.1063/1.4958699>
8. R. Hummatov, J.A. Hall, G.B. Kim, S. Friedrich, R. Cantor, S.T.P. Boyd, *J. Low Temp. Phys.* (2018). <https://doi.org/10.1007/s10909-018-1946-8>
9. R. Hummatov, L.N. Le, J.A. Hall, S. Friedrich, R.A. Cantor, S.T.P. Boyd, *IEEE Trans. Appl. Supercond.* **27**(4), 2200205 (2017). <https://doi.org/10.1109/TASC.2016.2626918>
10. S.T.P. Boyd, R.H. Cantor, *AIP Conf. Proc.* **1185**, 595 (2009). <https://doi.org/10.1063/1.3292412>